Scripta Materialia 118 (2016) 46–50

Contents lists available at ScienceDirect

Scripta Materialia

journal homepage: www.elsevier.com/locate/scriptamat

Deformation of lamellar TiAl alloys by longitudinal twinning

Thomas Edward James Edwards, Fabio Di Gioacchino *, Rocío Muñoz-Moreno, William John Clegg

Department of Materials Science and Metallurgy, 27 Charles Babbage Rd, University of Cambridge, Cambridge CB3 0FS, UK

ARTICLE INFO

Article history:
Received 9 December 2015
Received in revised form 1 March 2016
Accepted 4 March 2016
Available online 24 March 2016

Keywords:
Titanium aluminide
Twinning
Microindentation
Electron backscattering diffraction (EBSD)
Digital image correlation

ABSTRACT

The occurrence of longitudinal twinning in the engineering alloy Ti-45Al-2Nb-2Mn (at.%)-0.8 vol.% TiB_2 has been studied by measuring the changes in crystallographic orientation within individual lamellae during microcompression. Twinning in this alloy appeared to be a nucleation-limited process with the twins growing from lamellar boundaries at resolved shear stresses as low as 100 MPa, consistent with observations elsewhere. However, instead of forming twins ~10–200 nm in thickness, as in polysynthetically twinned crystals, the longitudinal twins in this alloy were initiated at a lamellar boundary and then spread through the whole lamella.

γ-TiAl and α_2-Ti_3Al have insufficient slip systems to allow a general plastic strain at a lamellar boundary [1,2]. Dislocation glide [3,4] or twinning [5] at such boundaries will therefore be associated with elastic misfit strains. These can be relaxed by the formation of cracks [6], which can then grow by fatigue. Preventing the formation of such flaws requires a quantitative understanding of the possible deformation modes. Initial work [7] focused on dislocation glide and on twinning, where the twin is at an angle to the lamella interface, *transverse twinning* [8,9] operating on the $\{111\}\langle 11\bar{2}]$[1] system.

However, there has also been a considerable body of work on macroscopic polysynthetically twinned (PST) crystals [10–13]. After deformation, such crystals show lamellae ~10–200 nm in thickness [10,12–14], parallel with the lamella boundaries and in a twin orientation to the surrounding material, causing a refinement of the lamellar spacing [11–13]. This *longitudinal twinning* [2,9] also operates on the $\{111\}\langle 11\bar{2}]$ system.

More recently, there has been considerable interest in using microcompression to determine local mechanical properties, effects of size and critical resolved shear stresses of γ-TiAl [15–17]. Such techniques have the potential to study longitudinal twinning directly, from the changes in orientation that occur during deformation.

However, there are complications with this, for as Fujiwara [10] has pointed out, adjacent lamellae in a PST crystal are in twin orientations, either true twin orientations or other variants. The aim of this paper therefore is to make direct observations of longitudinal twinning in a commercial alloy Ti-45Al-2Nb-2Mn (at.%)-0.8 vol.% TiB_2 (Ti4522XD), relating these to features on the stress/strain curve. This requires techniques for mapping the orientation of the crystal lattice in the same region both before and after deformation.

The crystal orientation changes of the lamellae, after compressive deformation of TiAl micropillars ion-milled from a single colony with defined lamellar orientations with respect to the loading axis, $15° < \Phi < 75°$, *soft-mode* [5,11], were established using electron backscatter diffraction (EBSD). The refined accuracy method [18] for reliable indexing of γ-TiAl variants was employed. The test pieces were made sufficiently small that some would not incorporate domain boundaries; hence longitudinal twins could be unconstrained. Digital image correlation (DIC) was used for identifying where dislocation glide occurred, particularly adjacent to twinned lamellae.

Samples $2 \times 3 \times 8$ mm^3 of Ti4522XD were ground and polished to a colloidal silica finish at the top surface and an adjacent side face. After polishing, back-scattered electron (BSE) imaging was used to identify colonies where lamellae were perpendicular to the side face of the sample and at an angle $15° < \Phi < 75°$ to its top surface, Fig. 1(a). Micropillars of 5×5 μm^2 section with a maximum taper of 2° and aspect ratio of 2.5 were Ga + ion-milled on the edge of such colonies to avoid shadowing of the EBSD patterns. The top surface of the micropillars was also milled to ensure that it was perpendicular to the pillar axis. To identify the effects of scatter, two or three micropillars were made in each of the six colonies investigated, with one pillar per colony undergoing the complete EBSD and DIC analysis.

A low 2 kV milling step improved the surface finish for EBSD, which was carried out with 40 nm step size. This caused some rounding of the front corners that could have later hampered the testing. To restore sharp corners, an additional layer <500 nm thick was removed, Fig. 1(b). A Pt speckle pattern was then deposited on the exposed side

* Corresponding author.
E-mail address: fd302@cam.ac.uk (F. Di Gioacchino).

[1] This notation is employed to reflect the tetragonal symmetry of γ-TiAl; $\langle 11\bar{2}]$ indicates that the first two indices are permutable, but the third is not.

http://dx.doi.org/10.1016/j.scriptamat.2016.03.004

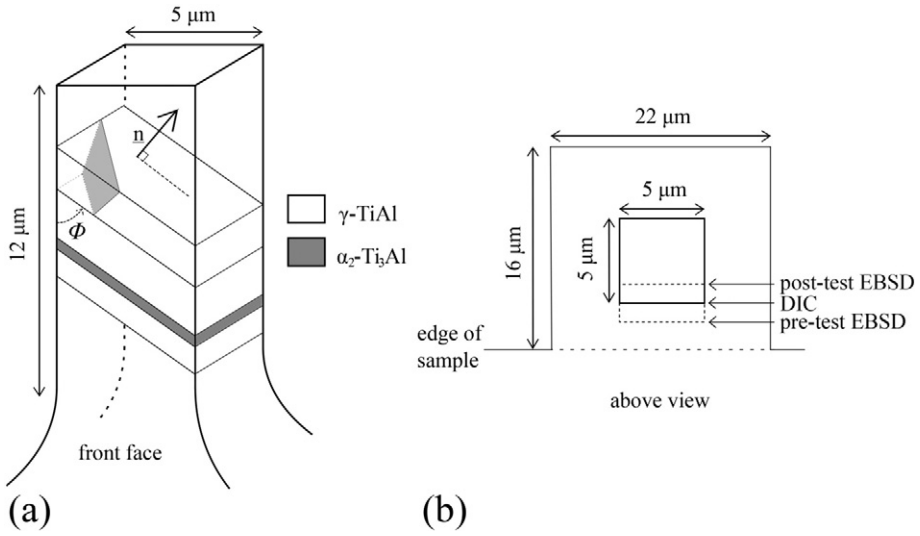

Fig. 1. (a) Drawing showing the angle Φ between lamellae and the pillar axis, and the potential orientation of a domain boundary, light grey, into the pillar depth (b) milling treatments for sequential EBSD and DIC steps.

of the pillar in a dual beam FIB/SEM (Helios NanoLab, FEI, USA) and a series of high-resolution scanning electron microscopy (SEM) images acquired to map the surface strain by DIC [19].

Micropillars were compressed uniaxially at room temperature by a 10 μm diamond punch (Synton, Switzerland) in an SEM nanoindenter (Alemnis, Switzerland) under displacement control, enabling the study of post-yield deformation. Monotonic loading to ~10% strain was followed by immediate unloading, at 0.05 μm s^{-1}, equivalent to a strain rate of ~4 × 10^{-3} s^{-1}. Progressive loading with complete unloading between steps was also performed. The test data was corrected for rig compliance. The videos of the compression tests are included in the supplementary data.

After testing, the surface strains were remeasured. Correlation of pre- and post-deformation images was performed using the DIC software (DaVis, LaVision, Germany), with a subset size of 16 × 16 pixels, giving a resolution of 108 × 108 nm^2, using a 25% overlap. Information on lattice rotation, θ_3, at the pillar surface was extracted, as described elsewhere [19]. The Pt speckles were removed by a further <500 nm thick layer being milled from the front face to enable a second series of EBSD scans, Fig. 1(b). In order to identify true twin transformations [9], the specific interfacial plane of a given $\{111\}_\gamma$ was determined from the Euler angles of a given lamella in the orientation prior to deformation, using the crystallographic visualisation software Vesta [20] and the trace of the interface plane. To avoid systematic errors related to rigid body rotations upon sample positioning in the SEM, and as a result of pillar rotation during compression, comparisons were made between adjacent material in the appropriate matrix-twin orientations, taken from the same either pre- or post-deformation map. Operations with rotations, including calculations of the Schmid factors, were performed using MTex [21].

Transmission electron microscopy (TEM) was also employed to study the finer scale microstructures. FIB thinned slices of pillars after

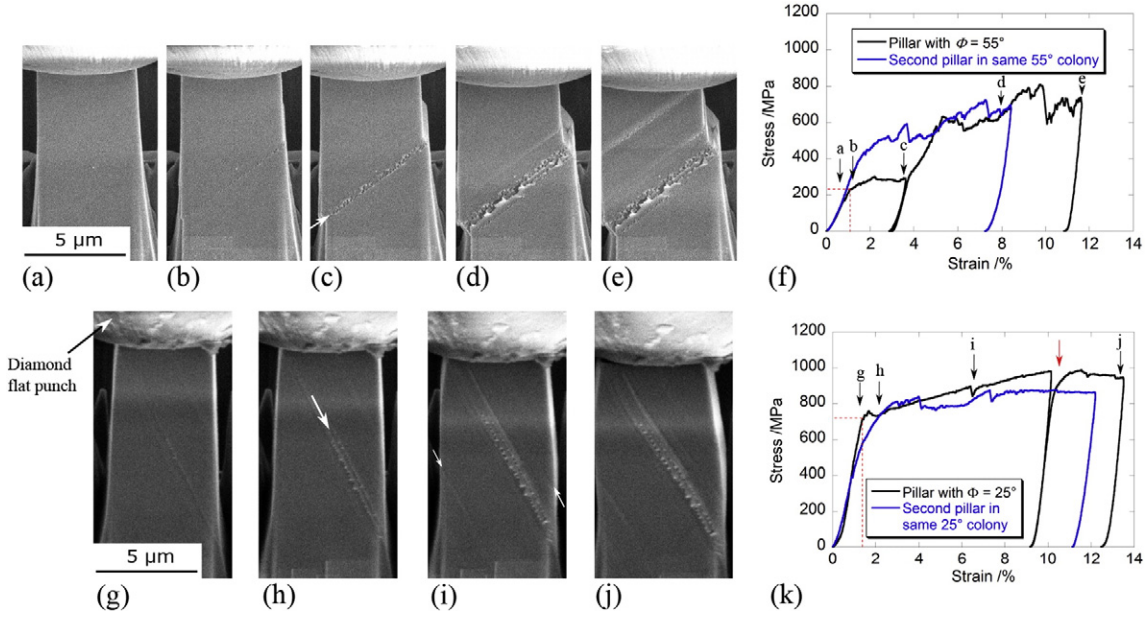

Fig. 2. Secondary SEM video frames: (a)–(e) $\Phi = 55°$ micropillar, (g)–(j) $\Phi = 25°$ micropillar, with loading curves (f) and (k), respectively. The white arrows in (c) and (h) correspond to the location of the longitudinal twinning indentified by EBSD and in (i) of slip bands observed in DIC. When the sample was loaded and then completely unloaded, deformation started at a lower stress than had been previously applied, red arrow in Fig. 2(k).

compression were imaged in a 200 kV, FEG source TEM (Tecnai F20, FEI, USA) fitted with a CCD camera.

Events taking place during compression of a micropillar with $\Phi = 55°$ are shown in Fig. 2(a)–(e) and could be related to the stress–strain curve, shown as a black line in Fig. 2(f). The first plastic deformation occurs by a progressively thickening band parallel to the lamellae, as observed by surface relief contrast. Small differences in the stress/strain curves for pillars within a same colony were seen, Fig. 2(f). Different proportions of α_2, a range of lamellar thicknesses and domain boundaries may all contribute to these.

The pre- and post-compression EBSD orientation maps for the $\Phi = 55°$ pillar are shown in Fig. 3(a) and (b), along with a colour key to identify the γ-TiAl variant twin pairs [12]. α_2-Ti_3Al could be readily identified from the compositional contrast of a BSE image and this was used as a guide in locating and overlaying the EBSD data. The Euler angles (Bunge) for material in the matrix orientation I_M, lamella 1, in the pillar in Fig. 3(a) were $\varphi_{I_M} = 158.6°$, $\vartheta_{I_M} = 83.5°$ and $\Psi_{I_M} = 47.6°$. This gave the interfacial plane as $(1\bar{1}1)_\gamma$. After conversion to quaternion representation [19,22], $q_{I_M} = (q_0, \boldsymbol{q})$, a 180° rotation, r_T, of the crystal orientation before deformation was performed about the $(1\bar{1}1)_\gamma$ plane normal to yield the orientation expected, $q_{I_T\ expc}$, if longitudinal twin I_T were to form:

$$q_{I_T\ expc} = r_T q_{I_M} \tag{1}$$

The misorientation angle, Δα, between $q_{I_T\ expc}$ and the measured crystal orientation ($\varphi_{I_T} = 89.1°$, $\vartheta_{I_T} = 90.5°$ and $\Psi_{I_T} = 51.7°$, for the latter), $q_{I_T\ meas}$, was calculated as:

$$\Delta\alpha = 2 \cdot \arccos(\Delta q_0) \tag{2}$$

with

$$\Delta q = q_{I_T}^{-1}{}_{expc} \quad q_{I_T\ meas} \tag{3}$$

Here, this misorientation, $\Delta\alpha = 0.9°$, was low, indicating that longitudinal twinning had occurred (I_M twins to I_T).

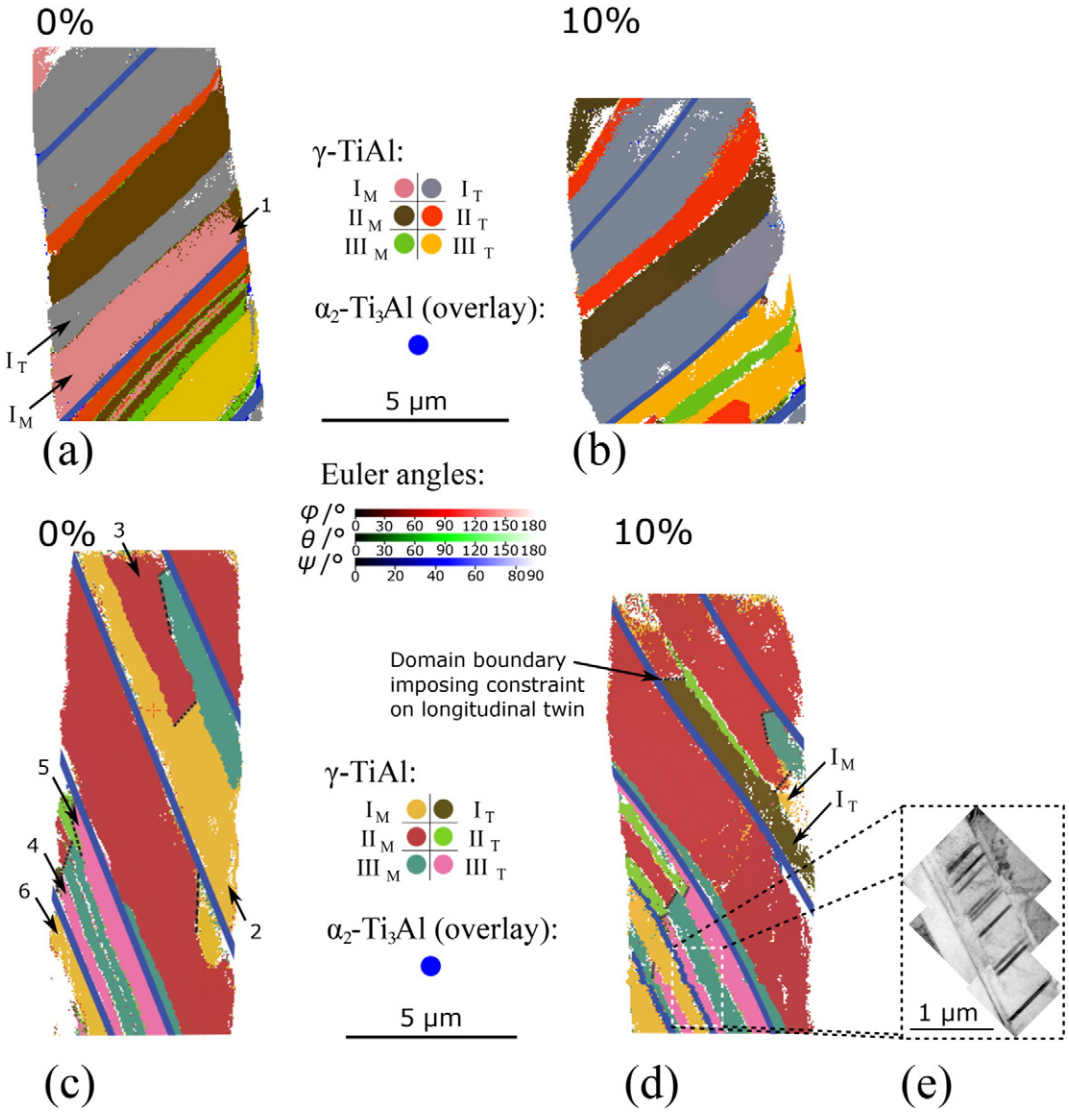

Fig. 3. Orientation mapping by EBSD of the $\Phi = 55°$ pillar (a) before and (b) after testing with overlay of the α_2-Ti_3Al lamellae (blue), similarly for the $\Phi = 25°$ pillar in (c) and (d). Arrows point to the region of longitudinal twinning. Domain boundaries are shown in (c) and (d) by black dashed lines, and their displacement can be associated to the sequential milling, Fig. 1(a) and (b). Bright field TEM image in the dashed white rectangle show transverse twinning had occurred. In (a) and (d), I_M and I_T indicate the locations where crystal orientation data was taken to confirm changes corresponding to longitudinal twinning.

In the limit of the resolution provided by the SEM video, longitudinal twinning was consistently the first deformation mechanism to operate in soft-mode pillars, causing small load drops, Fig. 2(h). The uniaxial twin initiation stress, σ, was determined as the peak stress preceding these load drops. The load drops observed suggest that longitudinal twinning is nucleation-limited. This is consistent with the observation that longitudinal twins, in this alloy, grew from lamellar interfaces [8], possibly by the dissociation of misfit dislocations into twinning partials, as reported for transverse twinning in TEM studies [23]. It is also suggested by the lack of any load drop in the $\Phi = 55^\circ$ pillar, Fig. 2(f), where the pre-existing, twin-oriented neighbouring lamella would obviate the need for nucleation. In this case the twinning stress was determined as the first deviation from the elastic loading line.

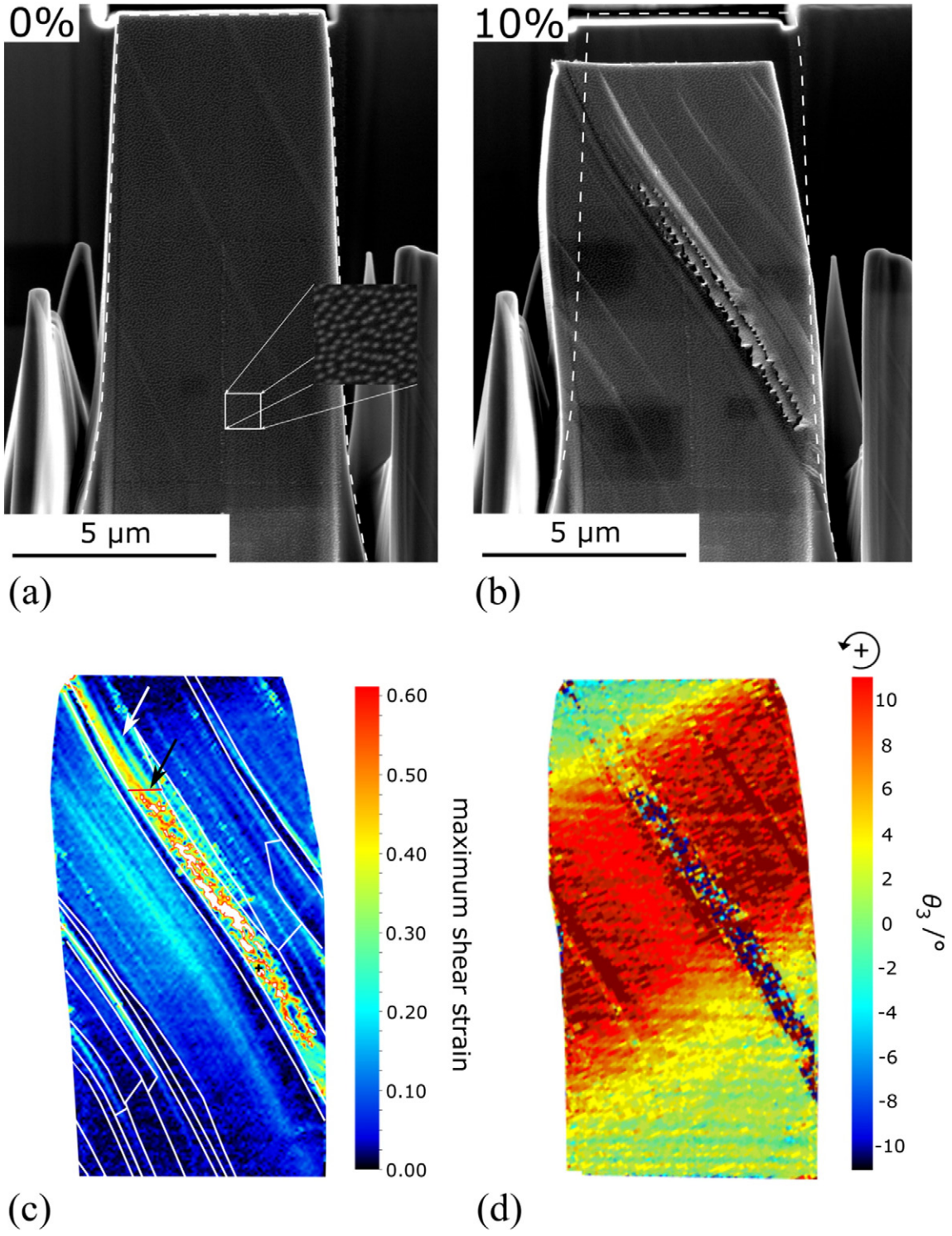

Fig. 4. High contrast secondary SEM images of the $\Phi = 25^\circ$ pillar with a surface Pt speckle pattern before and after compression to ~10% overall strain in (a) and (b). Maximum shear strain DIC maps with lamellar and domain boundaries overlaid in (c), and θ_3 (d). The diminishing slip bands in the domain ahead of the longitudinal twin in lamella 2 are white arrowed in (c), whilst the black arrow indicates the twin-constraining domain boundary, in red. Peeling of the Ga + damaged surface layer above longitudinal twins (b), yielding a low DIC confidence factor in those regions.

For this pillar, the resolved shear stress to initiate a longitudinal twin was estimated to be 106 MPa, using $\sigma = 234$ MPa, Fig. 2(f), and a Schmid factor of 0.45C.[2] (For other deformation mechanisms, the Schmid factors are reported in the Table in the supplementary material.) A total of five pillars all underwent longitudinal twinning that stretched the full width of the pillar, as in Fig. 3(a) and (b), giving the average resolved shear stress for the operation of the first unconstrained longitudinal twin as 100 ± 14 MPa. The value of 100 MPa obtained for the resolved shear stress required for the operation of unconstrained longitudinal twinning in γ-TiAl is, within error, equal to that for twinning in γ-TiAl single crystal microcompression samples [15], with a value of 113 MPa, and considerably less than the critical resolved shear stress for ordinary and super-dislocation glide [15]. The values of 100 MPa are slightly lower than those seen in early plasticity in lamellar TiAl, tested in the hard mode, where transverse twinning was the dominant deformation mechanism [16].

At higher temperatures, a value of 50 MPa, compared to 100 MPa here, was previously reported [12] as an apparent critical resolved shear stress for parallel twinning in soft-mode oriented PST crystals of Ti-48Al (at.%). The lower observed stress is consistent with the increased temperature [8,24–26] despite the reduced Al content and presence of Nb and Mn in the current alloy which are known to facilitate twinning [27].

However, the stress required for the onset of twinning increased if the growth of the longitudinal twin was constrained by a lamellar domain boundary, Fig. 2(g)–(j) and (k), 3(c) and (d). Here a value of 175 MPa was calculated for the $\Phi = 25°$ pillar, using $\sigma = 712$ MPa, Fig. 2(k), and a Schmid factor of 0.25C, where the longitudinal twinning of lamella 2 was constrained by a domain boundary. Twinning was again confirmed by a low $\Delta\alpha = 1.3°$. Post-mortem TEM & STEM bright-field imaging showed there was no cracking at such boundaries. Nevertheless, deformation mapping by DIC of SEM images in Fig. 4(a) and (b), indicated that longitudinal slip occurred in the domain ahead of the constrained twin, Fig. 4(c), which reduced with distance from the domain boundary. The transverse continuous band of (in-plane) lattice rotation, Fig. 4(d), shows that the lattice curvature associated with such reduction in slip intensity, i.e. slip gradients, is consistent with the overall lattice distortion of the pillar [19]. Additionally, in this pillar, the occurrence of longitudinal twinning in lamella 3 (II_M), Fig. 3(c), for which the Schmid factor equivalent was low, 0.11 in compression, see Table in supplementary material, is in a restricted region near the domain boundary; in other words, twinning of lamella 3 did not proceed to completion. Similarly, other pillars unloaded before the completion of twinning showed one or two longitudinal twins either side of the remaining parent lamella, with boundaries parallel to the original interfacial lamellar planes.

The nature of twinning is different in the engineering alloy studied here to that in PST crystals where the Al content is above 48 at.%. In PST crystals the longitudinal twins are ~10–200 nm thick [14]. However, in the alloy here, the twin spreads through the whole lamella, Fig. 3(a) and (d), so the initial lamella thickness determines the final twin thickness. This cannot be associated with a change in temperature as the observations of thin twins were also made at room temperature, suggesting that this is due to the differences in composition between the PST crystals and the alloy investigated here.

The higher resolution imaging by TEM allowed the identification of transverse twinning to have been active during compression of the micropillars, Fig. 3(e). However, it was observed that this was confined to the lower domain III_T of lamella 4, Fig. 3(c), in the constrained base of the pillar. It has been found [5] that the accommodation of transverse twinning strains occurs by dislocation emission into neighbouring lamella. These results showed that deformation occurred in the region ahead of the longitudinal twin, Fig. 4(c). The presence of such domain boundaries strengthens easy mode loaded lamellar TiAl, following a Hall–Petch type relationship, though lamellar interfaces were thought to be more effective [28]. This deformation could explain the absence of cracks at domain boundaries ahead of longitudinal twins. It contrasts with observations from experiments on multi-colony samples, where longitudinal twinning is associated with flaws at the colony boundaries, as at grain boundaries by twinning in near-γ duplex γ-TiAl [29].

This paper has demonstrated the occurrence of twinning parallel to the soft mode oriented lamellar interfaces in Ti4522XD, a commercial γ-TiAl alloy, by establishing the changes in lamellae crystallographic orientations after deformation.

Micropillar compression tests showed that longitudinal twinning can occur at resolved shear stresses as low as 100 MPa, less than that required for dislocation glide or transverse twinning. Longitudinal twinning appeared to start at lamellar interfaces and continued until the twin had grown through the lamella, in contrast with observations in PST crystals [14]. At domain boundaries, slip accompanies the twinning shear maintaining boundary cohesion, whereas at colony boundaries, this shear can cause the nucleation of defects that may then grow in fatigue.

Additional research data supporting this publication are available as 'supplementary files' at the journal's website. This includes video files of the microcompression experiments and a table of the Schmid factors. Supplementary data associated with this article can be found in the online version, at http://dx.doi.org/10.1016/j.scriptamat.2016.03.004

[2] The suffix C indicates that this mechanism is only operative in compression, following the tension-compression asymmetry of twinning.

Acknowledgements

The work was supported by the EPSRC/Rolls-Royce Strategic Partnership (EP/H500375/1). Alberto Palomares Garcia, Claire Davis and Robert Jones are acknowledged for discussions and help with the TEM respectively.

References

[1] R.V. Mises, ZAMM — Journal of Applied Mathematics and Mechanics/Zeitschrift für Angewandte Mathematik und Mechanik, 81928 161–185.
[2] E. Goo, Scr. Mater. 38 (1998) 1711–1716.
[3] F. Appel, P.A. Beaven, R. Wagner, Acta Metall. Mater. 41 (1993) 1721–1732.
[4] J.B. Singh, G. Molénat, M. Sundararaman, S. Banerjee, G. Saada, P. Veyssière, A. Couret, Philos. Mag. 86 (2006) 2429–2450.
[5] F. Appel, J.D.H. Paul, M. Oehring, in, Wiley-VCH Verlag & Co. KGaA, Weinheim, 2011, pp. xvi, (745 pp.).
[6] C. Gandhi, M.F. Ashby, Acta Metall. 27 (1979) 1565–1602.
[7] D. Shechtman, M.J. Blackburn, H.A. Lipsitt, Metall. Trans. 5 (1974) 1373–1381.
[8] F. Appel, U. Brossmann, U. Christoph, S. Eggert, P. Janschek, U. Lorenz, J. Müllauer, M. Oehring, J.D.H. Paul, Adv. Eng. Mater. 2 (2000) 699–720.
[9] R. Lebensohn, H. Uhlenhut, C. Hartig, H. Mecking, Acta Mater. 46 (1998) 4701–4709.
[10] T. Fujiwara, A. Nakamura, M. Hosomi, S.R. Nishitani, Y. Shirai, M. Yamaguchi, Philos. Mag. A 61 (1990) 591–606.
[11] H. Inui, M.H. Oh, A. Nakamura, M. Yamaguchi, Acta Metall. Mater. 40 (1992) 3095–3104.
[12] H.Y. Kim, K. Maruyama, Acta Mater. 49 (2001) 2635–2643.
[13] H.Y. Kim, K. Maruyama, Trans. Nonferrous Metals Soc. China 12 (2002) 561–568.
[14] K. Kishida, H. Inui, M. Yamaguchi, Philos. Mag. A 78 (1998) 1–28.
[15] K. Fujimura, K. Kishida, K. Tanaka, H. Inui, in: M. Palm, B. Bewlay, S. Kumar, K. Yoshimi (Eds.), MRS Online Proceedings Library, Materials Research Society, Boston, USA 2011, pp. 201–206.
[16] M. Rester, F.D. Fischer, C. Kirchlechner, T. Schmoelzer, H. Clemens, G. Dehm, Acta Mater. 59 (2011) 3410–3421.
[17] W.J. Porter, M.D. Uchic, R. John, N.B. Barnas, Scr. Mater. 61 (2009) 678–681.
[18] K. Thomsen, N.H. Schmidt, A. Bewick, K. Larsen, J. Goulden, Microsc. Microanal. 19 (2013) 724–725.
[19] F. Di Gioacchino, W.J. Clegg, Acta Mater. 78 (2014) 103–113.
[20] K. Momma, F. Izumi, J. Appl. Crystallogr. 44 (2011) 1272–1276.
[21] F. Bachmann, R. Hielscher, H. Schaeben, Solid State Phenom. 160 (2010) 63–68.
[22] W. Pantleon, Scr. Mater. 58 (2008) 994–997.
[23] F. Appel, Philos. Mag. 85 (2005) 205–231.
[24] J.W. Christian, S. Mahajan, Prog. Mater. Sci. 39 (1995) 1–157.
[25] H.A. Lipsitt, D. Shechtman, R.E. Schafrik, Metall. Trans. A 6 (1975) 1991–1996.
[26] Y.Q. Sun, P.M. Hazzledine, J.W. Christian, Philos. Mag. A 68 (1993) 471–494.
[27] K. Kothari, R. Radhakrishnan, N.M. Wereley, Prog. Aerosp. Sci. 55 (2012) 1–16.
[28] Y. Umakoshi, T. Nakano, Acta Metall. Mater. 41 (1993) 1155–1161.
[29] B.A. Simkin, B.C. Ng, M.A. Crimp, T.R. Bieler, Intermetallics 15 (2007) 55–60.